

# Flat optical conductivity in topological kagome magnet $\text{TbMn}_6\text{Sn}_6$

R. S. Li,<sup>1,\*</sup> Tan Zhang,<sup>2,\*</sup> Wenlong Ma,<sup>1</sup> S. X. Xu,<sup>1</sup> Q. Wu,<sup>1</sup> L. Yue,<sup>1</sup> S. J. Zhang,<sup>1</sup> Q. M. Liu,<sup>1</sup> Z. X. Wang,<sup>1</sup> T. C. Hu,<sup>1</sup> X. Y. Zhou,<sup>1</sup> D. Wu,<sup>3</sup> T. Dong,<sup>1</sup> Shuang Jia,<sup>1,4,5</sup> Hongming Weng,<sup>2,6,7,8,†</sup> and N. L. Wang<sup>1,3,4,‡</sup>

<sup>1</sup>International Center for Quantum Materials, School of Physics, Peking University, Beijing 100871, China

<sup>2</sup>Beijing National Laboratory for Condensed Matter Physics,

Institute of Physics, Chinese Academy of Sciences, Beijing 100190, China

<sup>3</sup>Beijing Academy of Quantum Information Sciences, Beijing 100913, China

<sup>4</sup>Collaborative Innovation Center of Quantum Matter, Beijing 100871, China

<sup>5</sup>CAS Center for Excellence in Topological Quantum Computation,

University of Chinese Academy of Sciences, Beijing 100190, China

<sup>6</sup>School of Physical Sciences, University of Chinese Academy of Sciences, Beijing 100049, China

<sup>7</sup>Songshan Lake Materials Laboratory, Dongguan, Guangdong 523808, China

<sup>8</sup>CAS Center for Excellence in Topological Quantum Computation, Beijing 100190, China

(Dated: July 21, 2022)

Kagome magnet  $\text{TbMn}_6\text{Sn}_6$  is a new type of topological material that is known to support exotic quantum magnetic states. Experimental work has identified that  $\text{TbMn}_6\text{Sn}_6$  hosts Dirac electronic states that could lead to topological and Chern quantum phases, but the optical response of the Dirac fermions of  $\text{TbMn}_6\text{Sn}_6$  and its properties remain to be explored. Here, we perform optical spectroscopy measurement combined with first-principles calculations on single-crystal sample of  $\text{TbMn}_6\text{Sn}_6$  to investigate the associated exotic phenomena.  $\text{TbMn}_6\text{Sn}_6$  exhibits a frequency-independent optical conductivity spectra in a broad range from 1800 to 3000  $\text{cm}^{-1}$  (220-370 meV) in experiments. The theoretical band structures and optical conductivity spectra are calculated with several shifted Fermi energy to compare with the experiment. The theoretical spectra with 0.56 eV shift for Fermi energy are well consistent with our experimental results. Besides, the massive quasi-two-dimensional (quasi-2D) Dirac bands, which have linear band dispersion in  $k_x$ - $k_y$  plane and no band dispersion along the  $k_z$  direction, exist close to the shifted Fermi energy. According to tight-bond model analysis, we find that quasi-2D Dirac bands give rise to a flat optical conductivity, while its value is smaller than the result by calculations and experiments. It indicates that the other trivial bands also contribute to the flat optical conductivity.

## I. INTRODUCTION

Kagome material has attracted immense interest due to its special crystal structure, which serves as an important platform to investigate the interplay among magnetism, electron correlation effects, and topological order [1–5]. The kagome lattice has a corner-sharing triangles network and it is predicted to have dispersionless bands and band singularities (van Hove singularities). Many intriguing novel phenomena and properties, such as anomalous Hall effect [6–9], topological Dirac states [10], quantum spin liquid states [11, 12], charge density wave, and superconductivity [13] have been discovered in those materials. In a kagome lattice, combining ferromagnetic (FM) ordering with strong spin-orbit coupling (SOC) can break time-reversal symmetry [3], which yields nontrivial topological states. Intrinsic anomalous Hall effect can arise from the integration of Berry curvature over the Brillouin zone (BZ) [6]. Additionally, kagome magnets with broken time-reversal symmetry are supposed to be an attractive candidate for the realization of the spinless Haldane model [2, 3]. The discovery of superconductivity

and charge density wave in the kagome material  $\text{CsV}_3\text{Sb}_5$  promises to be important progress in condensed-matter physics [13, 14]. It is confirmed that the kagome lattice is a fertile platform to explore novel states and phase behaviors.

Recently, the transition-metal-based kagome magnet  $\text{RMn}_6\text{Sn}_6$  (where R is a rare earth element) family has been studied extensively in the context of magnetism-induced various topological states and phase behaviors [15–25]. This class of materials is predicted to support the nontrivial topological states owing to a pristine Mn-base kagome layer with weak interlayer coupling. While Mn atoms form magnetic kagome lattice, R atoms also contribute to magnetization, which plays a significant role in topological properties of  $\text{RMn}_6\text{Sn}_6$  [16, 26]. As all of the atom moments contribute to net  $c$ -axis ferromagnetic ordering without any magnetic impurities,  $\text{TbMn}_6\text{Sn}_6$  is an ideal system to search for the Chern gapped topological fermions. As a recent article reported,  $\text{TbMn}_6\text{Sn}_6$  can host Landau quantization on the application of a 9 T magnetic field, which is a moderate magnetic field for kagome material to reach quantum limit [15].

$\text{TbMn}_6\text{Sn}_6$  has a layered hexagonal crystal structure, with a manganese kagome layer stacked along the  $c$ -axis. Out-of-plane ferrimagnetic order can arise from anti-parallel coupled magnetic coupling between Tb and Mn moment below Curie temperature  $T_c = 423$  K [27, 28]. Due to a net magnetization and SOC, Dirac bands open

\* These authors contributed equally to this work.

† [hmweng@iphy.ac.cn](mailto:hmweng@iphy.ac.cn)

‡ [nlwang@pku.edu.cn](mailto:nlwang@pku.edu.cn)

a gap at the crossing points that gives rise to the correlated massive Dirac fermions. Combining scanning tunneling microscope (STM) and angle-resolved photoemission spectroscopy (ARPES) measurements,  $\text{TbMn}_6\text{Sn}_6$  indeed host linear dispersions near the zone corners with a Chern gap above the Fermi level. The energy from the top of the lower Dirac branch to the Fermi level is about 130 meV, while the Chern gap  $\Delta$  is about 34 meV [15]. Massive Dirac fermions generate large Berry curvature that induces intrinsic anomalous Hall effect. In addition, quantum oscillation data indicated that this Fermi surface in the bulk crystal is two-dimensional like [15, 19]. However, because of the complex Mn-3d electron correlation effect, density function theory calculations could not give accurate energy bands structure, where the calculated location of Dirac point is not consistent with the STM results [23, 24]. In the work of Yin et al [15], the calculated Fermi level has an implicit shift of 0.56 eV to match the experimental results, which is not a common case. Considering the effect of Mn-3d electron correlation, the quasi-2D Dirac cone at 0.7 eV above the Fermi level shifts down to 0.3 eV [23], but it's still far away from the Fermi level to have a dominant contribution to the electrical response. Using density functional theory plus dynamical mean-field theory (DFT + DMFT), the calculated electronic structures of  $\text{YMn}_6\text{Sn}_6$  were consistent with experimental results measured by ARPES [18], indicating that this method of calculation may well approximate the electronic structure of this class materials. Furthermore, the Berry curvature of all the occupied states should contribute anomalous Hall effect. It is not reasonable to attribute all the topological features to the single Dirac cone at the  $K$  point, especially when this Dirac cone is far from the Fermi level based on the raw calculation results [23]. Despite these experimental and theoretical works, the electronic structure and optical response of  $\text{TbMn}_6\text{Sn}_6$  remain to be explored. The real position of Dirac point needs to be acquired by direct experiment probes, which is important to understand the correlation effects. On the other hand, while most bands near the Fermi level are highly dispersive,  $\text{TbMn}_6\text{Sn}_6$  exhibit quasi-2D transport behaviors [19]. It is highly interesting to investigate the unusual electronic properties of  $\text{TbMn}_6\text{Sn}_6$ , which can elucidate the quantum nature of this kagome magnet.

In this work, we systematically investigate the underlying physics of kagome lattice  $\text{TbMn}_6\text{Sn}_6$  by combining optical spectroscopy and first-principles calculations. Optical spectroscopy is a valuable and important method that probes charge dynamics and the electronic band structures of materials. Owing to the deeper penetration of light in the infrared range, optical spectroscopy reflects the bulk properties of a material, while STM and ARPES are sensitive to the surface. Additionally, the Dirac points and most dispersionless bands of  $\text{TbMn}_6\text{Sn}_6$  are above the Fermi level and couldn't be detected by ARPES. Compared with the ARPES measurements, the advantage of optical probe is that it can measure the

inter-band transition from the occupied state to the unoccupied state. As is known, when a system consists of Dirac fermions, the real part of the optical conductivity ( $\sigma = \sigma_1 + i\sigma_2$ ) is supposed to follow a power law, i.e.  $\sigma_1 \sim \omega^{d-2}$  (where  $d$  is dimension of the system) [29–31]. The power law is a compelling tool to investigate the properties of Dirac fermions and has indeed been confirmed in various systems. For 2D Dirac semimetal  $\text{Fe}_2\text{Sn}_3$  [32] and 2D Dirac nodal line semimetal  $\text{ZrSiS}$  [33], the optical conductivity is independent with frequency. On the other hand, 3D Dirac semimetal  $\text{ZrTe}_5$  [34],  $\text{NbAs}_2$  [35], and 3D Weyl semimetal  $\text{Co}_3\text{Si}_2\text{S}_2$  [36] display linear optical conductivity.

## II. EXPERIMENTAL RESULTS

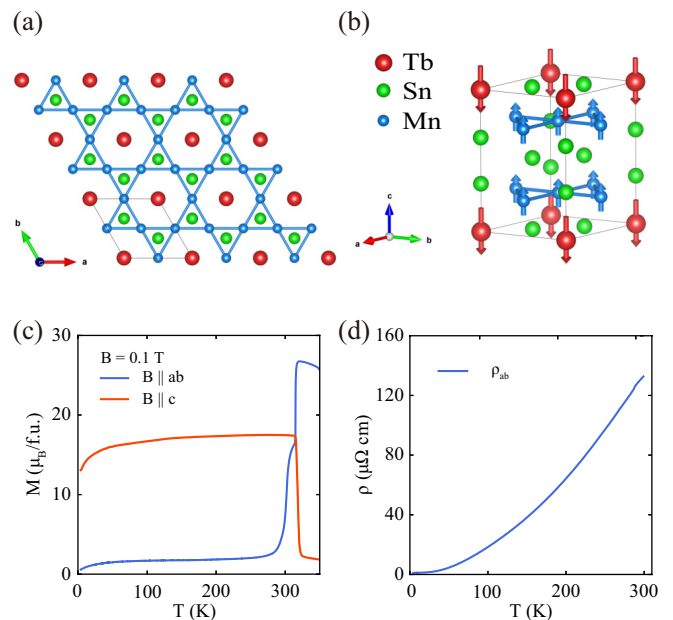


FIG. 1. Crystal structure, magnetic susceptibility, and resistivity in  $\text{TbMn}_6\text{Sn}_6$ . (a) Crystal of  $\text{TbMn}_6\text{Sn}_6$  within a unit cell is shown by the gray solid lines. (b) Side view of the structure with the orientation of the Tb and Mn magnetic moments below 315 K. (c) The temperature-dependence magnetic susceptibility with a zero-field-cooling mode at  $B = 0.1$  T for  $B \parallel ab$  and  $B \parallel c$ . (d) The dc-resistivity of  $\text{TbMn}_6\text{Sn}_6$  as a function of temperature.

$\text{TbMn}_6\text{Sn}_6$  has a layered structure with space group  $P6/Pmmn$  and hexagonal lattice constants of  $a = b = 5.5$  Å,  $c = 9$  Å. It is formed by stacking of  $\text{TbSn}_2$ - $\text{Mn}_3$ - $\text{Sn}$ - $\text{Sn}_2$ - $\text{Sn}$ - $\text{Mn}_3$ - $\text{TbSn}_2$  layers along the  $c$ -axis, as shown in Figs. 1(a) and (b). Mn atoms form pristine kagome layers, which are distinguished from the kagome lattice containing additional atoms in other well-known kagome magnets, including  $\text{CsV}_3\text{Sb}_5$ ,  $\text{Co}_3\text{Sn}_2\text{S}_2$  and  $\text{Fe}_2\text{Sn}_3$ .  $\text{TbMn}_6\text{Sn}_6$  orders in a collinear in-plane ferromagnetic spin structure below Curie temperature ( $T_c$

= 423 K). With the decrease in temperature, it manifests a spin reorientation at about 315 K, where the *ab*-plane aligned moments are flopped to be parallel to the *c*-axis [24, 27, 28], as reflected in the magnetic susceptibility anisotropy in Fig. 1(c). The temperature-dependent magnetization experiments were performed in field-cooled conditions under a magnetic field of 0.1 T applied out-of-plane and in-plane, respectively. Both susceptibilities measured along the *ab* plane and *c*-axis show a prominent change around 315 K, featuring the spin reorientation [24]. Below this temperature, all of the Mn moments are aligned on the *c*-axis with Tb moments anti-aligned along the *c*-axis. Figure 1 (d) shows the in-plane dc-resistivity as a function of temperature *T*, which was measured using a standard four-probe method in a Quantum Design physical property measurement system. In the entire measuring temperature range, the resistivity shows metallic behavior.

Figure 2 (a) displays the temperature-dependent in-plane reflectivity up to 5000  $\text{cm}^{-1}$ . Above 1800  $\text{cm}^{-1}$ , the change of temperature has only a minor influence on the reflectivity spectra. The low-energy reflectivity reaches almost unity. Additionally, when the temperature decreases, the low-energy reflectivity increases. Both features show that the sample has a highly metallic nature, in agreement with the resistivity measurement. The most significant feature in spectra  $R(\omega)$  is the substantial suppression in the midinfrared region. Upon cooling, there appears a dip gradually emerges between 800 and 1500  $\text{cm}^{-1}$ , which may indicate that this material opens a gap.

The real part of the optical conductivity  $\sigma_1(\omega)$  is derived from  $R(\omega)$  through the Kramers-Kronig relation, as displayed in Fig. 2(d). The Hagen-Rubens relation was used for the low-frequency extrapolation, and the X-ray atomic scattering functions were used in the high-frequency extrapolation. The optical conductivity  $\sigma_1(\omega)$  depends weakly on temperature *T* above 1800  $\text{cm}^{-1}$ . At low temperature, there is a sharp Drude peak at zero-frequency in conductivity. Then, a frequency-independent conductivity is followed by a step-like feature. Notably, the step-like structure gets broad at higher temperatures. The Drude peak at zero frequency narrows continuously with decreasing *T*, implying suppressed quasiparticle scattering.

The striking feature of the spectra is that the flat frequency-independent region in the range from 1800 to 3000  $\text{cm}^{-1}$  basically at all temperatures investigated. Naturally, such a typical signature is supposed to be the contribution of quasi-2D Dirac fermions as predicted by the power laws. Most of the Dirac energy bands arise from the spin-up  $d_{xy}$  and  $d_{x^2}$  orbitals of Mn atom, while temperature has a weaker effect on the magnetic moment of Mn [28]. Therefore, the energy bands have no significant change as temperature drops. Inter-band transitions start to contribute to the spectral weight from the mid-infrared range. The optical conductivity plateau nearly keeps the same at different temperatures, consist-

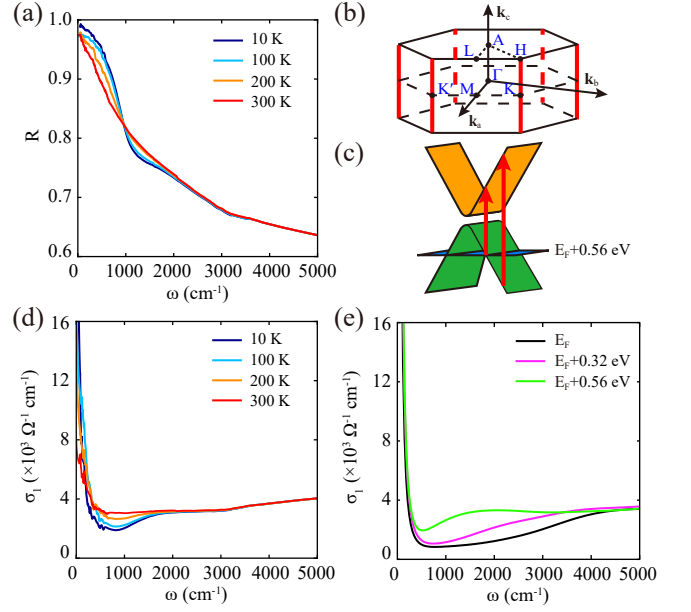


FIG. 2. (Color online) (a) Temperature-dependent optical reflectivity  $R(\omega)$ . (b) The bulk BZ of  $\text{TbMn}_6\text{Sn}_6$ . The red solid (dash) lines indicate the position of the nodal line. (c) The schematic diagram of the quasi-2D Dirac bands near the Fermi energy. The red arrows indicate the inter-band transition transitions. (d) The experimental optical conductivity  $\sigma_1(\omega)$  at different temperature. (e) The theoretical optical conductivity  $\sigma_1(\omega)$  at 0 K with shifts of Fermi energy.

ing the behavior of the energy bands varies with temperature. Since the Dirac band loses its linearity and other parabolic bands start to have a dominant contribution to the conductivity,  $\sigma_1(\omega)$  increases with frequency above 3000  $\text{cm}^{-1}$ .

To better understand the experimental results of  $\text{TbMn}_6\text{Sn}_6$ , the first-principles calculations are performed to simulate the band structures and optical conductivity. The  $\text{TbMn}_6\text{Sn}_6$  hosts the ferrimagnetic state at 0 K, where the effective magnetic moments on Tb and Mn atoms are along the *z*-axis but in the opposite direction, as shown in Figs. 1(b). The magnetization on Tb atom is contributed by the 4*f* orbitals which are away from the Fermi energy. To simplify the calculation, we treat the Tb-4*f* electrons as core electrons and do not consider them in the DFT calculation by using the pseudopotential which does not contain 4*f* electrons. The detailed calculation parameters are shown in Appendix B. Because the strong electron correlation effects of Mn-3*d* electrons in this material are hard to deal with in DFT level, we do not adopt the DFT+*U* method. To decrease the errors caused by ignoring strong correlation effects, we apply several energy shifts to the Fermi energy. We find a 0.56 eV shift of Fermi energy was applied in ref. 15, so we choose 0.32 and 0.56 eV shifts on the Fermi energy in our calculation.

The band structures in the  $k_z = 0$  plane without SOC are shown in Fig. 3(a). There are two Dirac points (DP1



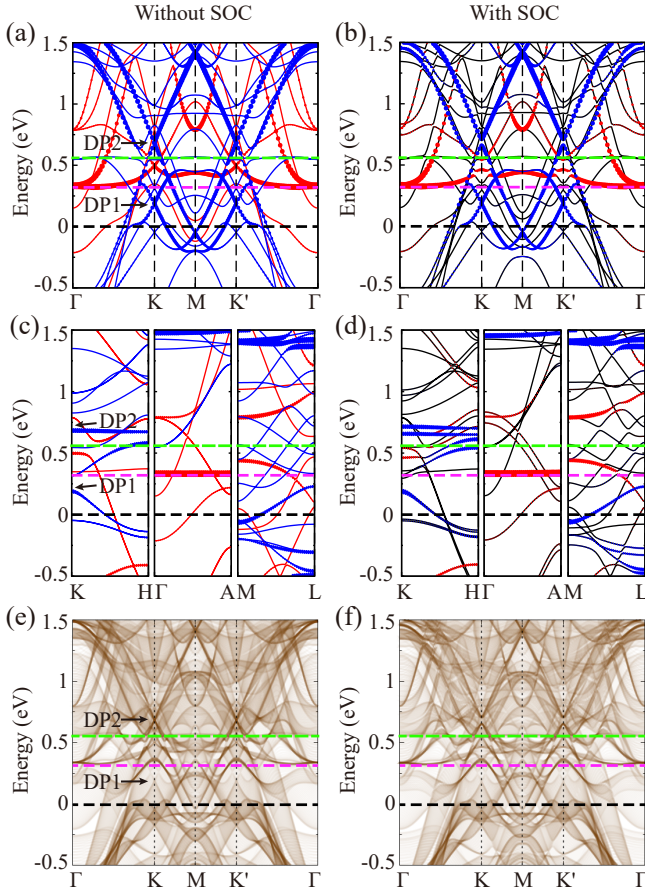


FIG. 3. (Color online) The band structures of  $\text{TbMn}_6\text{Sn}_6$  in the  $k_z = 0$  plane (a) without and (b) with SOC. The band structures along the  $k_z$  path (c) without and (d) with SOC. The red (blue) bands indicate the spin-up (spin-down) bands. The red (blue) circles indicate the projection weight of spin-up (spin-down) Mn  $d_{xy}$  and  $d_{x^2}$  orbitals. The band structures projected on the  $k_z = 0$  plane from band structures calculated in 50  $k_z$  planes from  $k_z = 0$  to  $k_z = 0.5k_c$  (e) without and (f) with SOC. The deeper brown color indicates the larger projection weight. Two Dirac cones (DP1 and DP2) at the  $K$  point are marked by arrows. The magenta and green dashed lines mark the 0.32 and 0.56 eV shift of Fermi energy

and DP2) at the energy of 0.187 and 0.682 eV located at  $K$  and  $K'$  points. They have linear band dispersion in the  $k_z = 0$  plane, which consists of Mn spin-up  $d_{xy}$  and  $d_{x^2}$  orbitals. The band structures along the  $k_z$  direction are shown in Fig. 3(c). It shows that the DP1 has a band dispersion along the  $k_z$  direction, while the DP2 has no band dispersion along the  $k_z$  direction. The DP2 makes up nodal lines with quasi-2D Dirac bands along the  $k_z$  direction and goes through the whole BZ. The position of nodal lines is indicated as six red solid (dash) lines in Fig. 2(b), which are related by  $C_6$  rotation symmetry. The projected band structures obtained by integrating the band structures in 50  $k_z$  planes from  $k_z = 0$  to  $k_z = 0.5k_c$  are shown in Fig. 3(e). The quasi-2D Dirac bands shown as deep brown color can be found at

$K$  and  $K'$  points. On considering SOC, the DP1 opens a small band gap (14 meV), while the DP2 opens a larger band gap (55 meV) at  $K$  and  $K'$  points as shown in Fig. 3(b). The Dirac points also open gaps along the  $k_z$  direction (Fig. 3(d)), but the band dispersion hardly change. The projected band structures with SOC are shown in Fig. 3(f). The quasi-2D Dirac bands shown as deep brown color open a gap of 55 meV. To verify our calculation results, the bands in the  $k_z = 0.3k_c$  and  $0.5k_c$  planes are calculated as shown in Appendix C.

The theoretical optical conductivity at 0 K is calculated based on the band structures. The detailed calculation formulas are introduced in Appendix B. The plasma frequency is calculated as  $\hbar\omega_p = 2.95$  eV. When the Fermi energy is shifted by 0.32 and 0.56 eV, the plasma frequency is calculated as 3.94 and 4.09 eV separately. The inverse lifetime  $\hbar\gamma$  is parameterized as 0.006 eV for all calculations. The theoretical optical conductivity spectra are shown in Fig. 2(e). The spectra contributed by intra-band transitions are mainly in the region from 0 to 1000  $\text{cm}^{-1}$ . When  $\omega \geq 1000$   $\text{cm}^{-1}$ , the spectra are dominated by the inter-band transitions. With the rising of Fermi energy, the spectra from inter-band transition gradually change from a linear dispersion with frequency to a step. When the Fermi energy is shifted by 0.56 eV, the theoretical spectra show a frequency-independent step existing from 1800 to 3000  $\text{cm}^{-1}$ , which are well consistent with the experimental spectra as shown in Fig. 2(d).

We think this step spectra could be contributed by the inter-band transitions between quasi-2D Dirac bands. According to previous researches, this optical conductivity can be calculated as an analytic formula by building the tight-binding model [33, 37–39]. The formula is

$$\sigma_1 = \frac{e^2 k_0}{16h} \times \Theta(\hbar\omega - \max\{\Delta, 2E\}), \quad (1)$$

where  $k_0$  is the total length of quasi-2D Dirac bands in momentum space,  $\Theta$  is the step function,  $\Delta$  is zero (the gap of Dirac cone) and  $E$  is the energy difference between the Fermi energy and the Dirac point (the midpoint of gap) for gapless (gapped) Dirac cone. For a gapless Dirac cone, the step-like optical conductivity exists from  $\hbar\omega = 0$  when the Dirac point locates at the Fermi energy. When the Dirac point is away from the Fermi energy, the step-like optical conductivity only arises when  $\hbar\omega \geq 2E$ , because the inter-band transitions are forbidden for low frequency ( $\hbar\omega < 2E$ ) due to Pauli blocking. For a gapped Dirac cone, the step-like optical conductivity arises when  $\hbar\omega \geq \Delta$  if the Fermi energy is in the gap ( $\Delta > 2E$ ), and it arises when  $\hbar\omega \geq 2E$  if the Fermi energy is away from the gap ( $\Delta \leq 2E$ ).

In our calculations for  $\text{TbMn}_6\text{Sn}_6$ , the gap of quasi-2D Dirac band is  $\Delta = 55$  meV, while the midpoint of the gap is  $E = 124$  meV beyond the shifted Fermi energy. It infers the start point of optical conductivity step is at  $2E = 248$  meV by the formula Eq. 1, which is consistent with that of 223 meV (1800  $\text{cm}^{-1}$ ) in our calculation. The optical conductivity value of the

step is also calculated by the formula. We calculate the  $k_0 = 1.4 \text{ \AA}^{-1}$  in the whole BZ, and the value of the step is estimated as  $\sigma_1 = 0.34 \times 10^3 \text{ \Omega}^{-1}\text{cm}^{-1}$ . It is smaller than the experimental result and theoretical result  $\sigma = 3.20 \times 10^3 \text{ \Omega}^{-1}\text{cm}^{-1}$ . We think the reason may be that Eq. 1 is a simple model to roughly estimate the conductivity plateau, and the other trivial bands near the shifted Fermi energy also contribute to constant optical spectra. We notice that the projected bands in Figs. 3 (e) and (f) also show a uniform band background except for the quasi-2D Dirac bands.

It should be noted that calculated conductivity values are closer to the experimental values after the Fermi energy is shifted upward by 0.56 eV, which is hard to understand. Surprisingly, the shifted Fermi energy is more in line with the previous experimental results, including STM, ARPES, and electrical transport measurement [15, 19]. Besides, a previous study has identified that  $\text{YMn}_6\text{Sn}_6$  hosts a quasi-2D Dirac cone at around 300 meV above the Fermi level measured by ARPES [18]. We can refer to this result since  $\text{TbMn}_6\text{Sn}_6$  and  $\text{YMn}_6\text{Sn}_6$  should have some similar band structures. We propose a possible explanation for this unusual case: The shift of the Fermi energy results in some compensation for the correlation effect of Mn atoms. Indeed, the calculation results suggest that the Dirac point at 0.7 eV above the Fermi level shifted down to 0.3 eV when considering the correlation effect [23]. More experiments will be needed to explore the nature of this compound.

### III. CONCLUSION

In summary, we have carried out comprehensive optical spectroscopy and theoretical calculations to investigate the electron properties of the  $\text{TbMn}_6\text{Sn}_6$  single crystal. The experimental optical conductivity spectra exhibit a frequency-independent step in a range from 1800 to 3000  $\text{cm}^{-1}$  (220-370 meV). When the Fermi level is shifted up by 0.56 eV, the theoretical spectra are well consistent with experimental results. The massive quasi-2D Dirac bands are found to exist close to the shifted Fermi energy by calculations, which could offer an ideal system to study the 2D topological quantum states. However, there are many complicated trivial bands existing. It leads to both quasi-2D Dirac bands and trivial bands contributing to the optical conductivity. With analytic calculation, the optical conductivity contributed by quasi-2D Dirac bands is obtained, which is smaller than that contributed by all bands.

### ACKNOWLEDGMENTS

This work was supported by the National Key Research and Development Program of China (No. 2017YFA0302904) and National Natural Science Foundation of China (No. 11888101).

## Appendix A: EXPERIMENT METHOD

High-quality single crystals of  $\text{TbMn}_6\text{Sn}_6$  were synthesized by the flux growth method as described elsewhere [40, 41]. The crystal has a flake-like shape with a shining a-b plane as the cleavage plane, consistent with its quasi-2D structure.

The in-plane reflectivity  $R(\omega)$  was measured by the Fourier transform infrared spectrometer Bruker 80 V in the frequency range from 50 to 32000  $\text{cm}^{-1}$ . At low frequencies, an in situ gold overcoating technique was used to get the reflection. Instead of gold, aluminum served as a reference above 8000  $\text{cm}^{-1}$ .

## Appendix B: CALCULATION METHOD

The First-principles calculations were performed to simulate the electronic structure of  $\text{TbMn}_6\text{Sn}_6$  by using the Vienna ab initio Simulation Package (VASP) [42–44]. The Perdew-Burke-Ernzerhof (PBE) exchange-correlation potential with the generalized gradient approximation (GGA) was used [45]. The projector augmented plane-wave pseudopotential was chosen in the calculations [46]. The cut-off energy was 500 eV and the reciprocal space was sampled by  $13 \times 13 \times 7$   $\Gamma$ -centered mesh for self-consistent calculation.

The optical conductive properties of the material were calculated based on the longitudinal expression of the dielectric matrix [47, 48]. The  $k$ -point sampling mesh is  $21 \times 21 \times 11$  mesh. The real part of optical conductivity is calculated by the formula:

$$\sigma_1(\omega) = \frac{\omega}{4\pi} \text{Im } \epsilon(\omega), \quad (\text{B1})$$

where dielectric function consists of inter-band and intra-band contributions,

$$\text{Im } \epsilon(\omega) = \text{Im } \epsilon_{\text{inter}}(\omega) + \text{Im } \epsilon_{\text{intra}}(\omega). \quad (\text{B2})$$

The imaginary part of inter-band dielectric function are calculated by the formula:

$$\begin{aligned} \text{Im } \epsilon_{\text{inter}}(\omega) = & \frac{8\pi^2 e^2}{V} \lim_{|\mathbf{q}| \rightarrow 0} \frac{1}{|\mathbf{q}|^2} \sum_{\mathbf{k}, v, c} |\langle u_{c, \mathbf{k}+\mathbf{q}} | u_{v, \mathbf{k}} \rangle|^2 \\ & \times \delta(\epsilon_{c, \mathbf{k}+\mathbf{q}} - \epsilon_{v, \mathbf{k}} - \hbar\omega). \end{aligned} \quad (\text{B3})$$

The intra-band contributions are calculated by the Drude model:

$$\text{Im } \epsilon_{\text{intra}}(\omega) = \frac{\gamma \omega_p^2}{\omega(\omega^2 + \gamma^2)}. \quad (\text{B4})$$

## Appendix C: THE BAND STRUCTURES IN THE OTHER $k_z$ PLANES

The band structures of  $\text{TbMn}_6\text{Sn}_6$  in the  $k_z = 0, 0.3k_c$  and  $0.5k_c$  planes with and without SOC are shown in the Fig. 4.

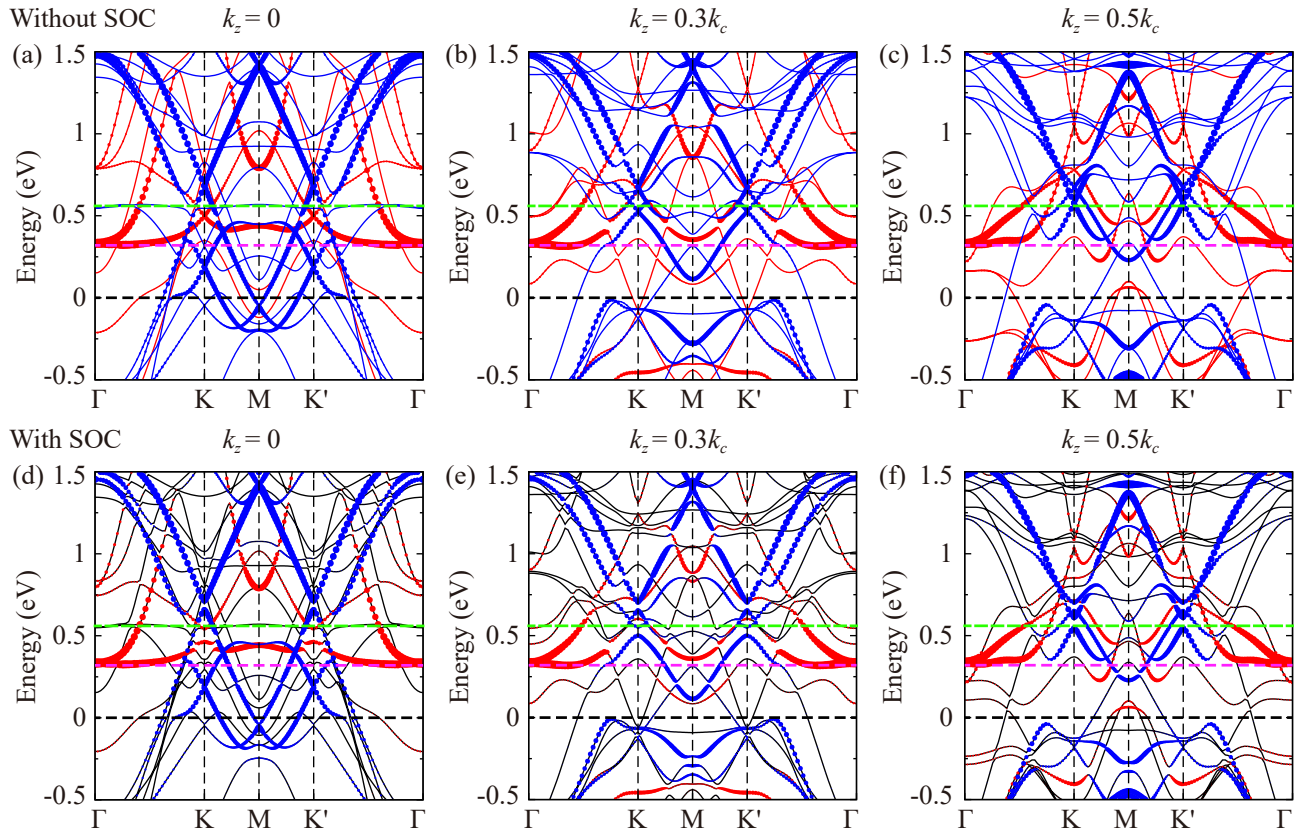


FIG. 4. (Color online) The band structures of  $\text{TbMn}_6\text{Sn}_6$  in the  $k_z = 0$  plane (a) without and (d) with SOC. The bands in  $k_z = 0.3k_c$  plane (b) without and (e) with SOC. The bands in  $k_z = 0.5k_c$  plane (c) without and (f) with SOC. The red (blue) circles indicate the projection weight of spin-up (spin-down) Mn  $d_{xy}$  and  $d_{x^2}$  orbitals. The magenta and green dashed lines mark the 0.32 and 0.56 eV shift of Fermi energy

- 
- [1] B. Keimer and J. Moore, *Nature Physics* **13**, 1045 (2017).
  - [2] F. D. M. Haldane, *Phys. Rev. Lett.* **61**, 15 (1988).
  - [3] G. Xu, B. Lian, and S.-C. Zhang, *Phys. Rev. Lett.* **115**, 186802 (2015).
  - [4] J.-X. Yin, S. S. Zhang, H. Li, K. Jiang, G. Chang, B. Zhang, B. Lian, C. Xiang, I. Belopolski, H. Zheng, *et al.*, *Nature* **562**, 91 (2018).
  - [5] J.-X. Yin, S. S. Zhang, G. Chang, Q. Wang, S. S. Tsirkin, Z. Guguchia, B. Lian, H. Zhou, K. Jiang, I. Belopolski, *et al.*, *Nature Physics* **15**, 443 (2019).
  - [6] F. D. M. Haldane, *Phys. Rev. Lett.* **93**, 206602 (2004).
  - [7] S. Nakatsuji, N. Kiyohara, and T. Higo, *Nature* **527**, 212 (2015).
  - [8] Q. Wang, S. Sun, X. Zhang, F. Pang, and H. Lei, *Phys. Rev. B* **94**, 075135 (2016).
  - [9] E. Liu, Y. Sun, N. Kumar, L. Muechler, A. Sun, L. Jiao, S.-Y. Yang, D. Liu, A. Liang, Q. Xu, *et al.*, *Nature physics* **14**, 1125 (2018).
  - [10] L. Ye, M. Kang, J. Liu, F. Von Cube, C. R. Wicker, T. Suzuki, C. Jozwiak, A. Bostwick, E. Rotenberg, D. C. Bell, *et al.*, *Nature* **555**, 638 (2018).
  - [11] Y. Zhou, K. Kanoda, and T.-K. Ng, *Rev. Mod. Phys.* **89**, 025003 (2017).
  - [12] L. Balents, *Nature* **464**, 199 (2010).
  - [13] B. R. Ortiz, L. C. Gomes, J. R. Morey, M. Winiarski, M. Bordelon, J. S. Mangum, I. W. H. Oswald, J. A. Rodriguez-Rivera, J. R. Neilson, S. D. Wilson, E. Ertekin, T. M. McQueen, and E. S. Toberer, *Phys. Rev. Materials* **3**, 094407 (2019).
  - [14] B. R. Ortiz, S. M. L. Teicher, Y. Hu, J. L. Zuo, P. M. Sarte, E. C. Schueller, A. M. M. Abeykoon, M. J. Krogstad, S. Rosenkranz, R. Osborn, R. Seshadri, L. Balents, J. He, and S. D. Wilson, *Phys. Rev. Lett.* **125**, 247002 (2020).
  - [15] J.-X. Yin, W. Ma, T. A. Cochran, X. Xu, S. S. Zhang, H.-J. Tien, N. Shumiya, G. Cheng, K. Jiang, B. Lian, *et al.*, *Nature* **583**, 533 (2020).
  - [16] W. Ma, X. Xu, J.-X. Yin, H. Yang, H. Zhou, Z.-J. Cheng, Y. Huang, Z. Qu, F. Wang, M. Z. Hasan, and S. Jia, *Phys. Rev. Lett.* **126**, 246602 (2021).
  - [17] W. Ma, X. Xu, Z. Wang, H. Zhou, M. Marshall, Z. Qu, W. Xie, and S. Jia, *Phys. Rev. B* **103**, 235109 (2021).
  - [18] M. Li, Q. Wang, G. Wang, Z. Yuan, W. Song, R. Lou, Z. Liu, Y. Huang, Z. Liu, H. Lei, *et al.*, *Nature Communications* **12**, 1 (2021).

- [19] X. Xu, J.-X. Yin, W. Ma, H.-J. Tien, X.-B. Qiang, P. Reddy, H. Zhou, J. Shen, H.-Z. Lu, T.-R. Chang, *et al.*, *Nature communications* **13**, 1 (2022).
- [20] H. Li, H. Zhao, K. Jiang, Q. Wang, Q. Yin, N.-N. Zhao, K. Liu, Z. Wang, H. Lei, and I. Zeljkovic, *Nature Physics*, 1 (2022).
- [21] S. X. M. Riberolles, T. J. Slade, D. L. Abernathy, G. E. Granroth, B. Li, Y. Lee, P. C. Canfield, B. G. Ueland, L. Ke, and R. J. McQueeney, *Phys. Rev. X* **12**, 021043 (2022).
- [22] H. Zhang, J. Koo, C. Xu, M. Sretenovic, B. Yan, and X. Ke, *Nature communications* **13**, 1 (2022).
- [23] Y. Lee, R. Skomski, X. Wang, P. Orth, A. Pathak, B. Harmon, R. McQueeney, and L. Ke, *arXiv preprint arXiv:2201.11265* (2022), 10.48550/ARXIV.2201.11265.
- [24] D. C. Jones, S. Das, H. Bhandari, X. Liu, P. Siegfried, M. P. Ghimire, S. S. Tsirkin, I. Mazin, and N. J. Ghimire, *arXiv preprint arXiv:2203.17246* (2022), 10.48550/ARXIV.2203.17246.
- [25] C. Mielke III, W. Ma, V. Pomjakushin, O. Zaharko, S. Sturniolo, X. Liu, V. Ukleev, J. White, J.-X. Yin, S. Tsirkin, *et al.*, *Communications Physics* **5**, 1 (2022).
- [26] G. Venturini, B. C. El Idrissi, and B. Malaman, *Journal of magnetism and magnetic materials* **94**, 35 (1991).
- [27] B. Malaman, G. Venturini, R. Welter, J. Sanchez, P. Vullet, and E. Ressouche, *Journal of Magnetism and Magnetic Materials* **202**, 519 (1999).
- [28] B. El Idrissi, G. Venturini, B. Malaman, and D. Fruchart, *Journal of the Less Common Metals* **175**, 143 (1991).
- [29] P. Hosur, S. A. Parameswaran, and A. Vishwanath, *Phys. Rev. Lett.* **108**, 046602 (2012).
- [30] A. Bácsi and A. Virosztek, *Phys. Rev. B* **87**, 125425 (2013).
- [31] C. J. Tabert, J. P. Carbotte, and E. J. Nicol, *Phys. Rev. B* **93**, 085426 (2016).
- [32] A. Biswas, O. Iakutkina, Q. Wang, H. C. Lei, M. Dressel, and E. Uykur, *Phys. Rev. Lett.* **125**, 076403 (2020).
- [33] M. B. Schilling, L. M. Schoop, B. V. Lotsch, M. Dressel, and A. V. Pronin, *Phys. Rev. Lett.* **119**, 187401 (2017).
- [34] R. Y. Chen, S. J. Zhang, J. A. Schneeloch, C. Zhang, Q. Li, G. D. Gu, and N. L. Wang, *Phys. Rev. B* **92**, 075107 (2015).
- [35] Y. Shao, Z. Sun, Y. Wang, C. Xu, R. Sankar, A. J. Breindel, C. Cao, M. M. Fogler, A. J. Millis, F. Chou, Z. Li, T. Timusk, M. B. Maple, and D. N. Basov, *Proceedings of the National Academy of Sciences* **116**, 1168 (2019).
- [36] R. Yang, T. Zhang, L. Zhou, Y. Dai, Z. Liao, H. Weng, and X. Qiu, *Phys. Rev. Lett.* **124**, 077403 (2020).
- [37] Y. Shao, Z. Sun, Y. Wang, C. Xu, R. Sankar, A. J. Breindel, C. Cao, M. M. Fogler, A. J. Millis, F. Chou, Z. Li, T. Timusk, M. B. Maple, and D. N. Basov, *Proceedings of the National Academy of Sciences* **116**, 1168 (2019), <https://www.pnas.org/doi/pdf/10.1073/pnas.1809631115>.
- [38] D. Santos-Cottin, M. Casula, L. de' Medici, F. Le Maréchal, J. Wyzula, M. Orlita, Y. Klein, A. Gauzzi, A. Akrap, and R. P. S. M. Lobo, *Phys. Rev. B* **104**, L201115 (2021).
- [39] J. P. Carbotte, *Journal of Physics: Condensed Matter* **29**, 045301 (2016).
- [40] P. C. Canfield and Z. Fisk, *Philosophical Magazine B* **65**, 1117 (1992).
- [41] D. Clatterbuck and K. Gschneidner, *Journal of Magnetism and Magnetic Materials* **207**, 78 (1999).
- [42] G. Kresse and J. Hafner, *Phys. Rev. B* **47**, 558 (1993).
- [43] G. Kresse and J. Hafner, *Phys. Rev. B* **49**, 14251 (1994).
- [44] G. Kresse and J. Furthmüller, *Computational Materials Science* **6**, 15 (1996).
- [45] J. P. Perdew, K. Burke, and M. Ernzerhof, *Phys. Rev. Lett.* **77**, 3865 (1996).
- [46] P. E. Blöchl, *Phys. Rev. B* **50**, 17953 (1994).
- [47] M. Gajdoš, K. Hummer, G. Kresse, J. Furthmüller, and F. Bechstedt, *Phys. Rev. B* **73**, 045112 (2006).
- [48] M. J. van Setten, S. Er, G. Brocks, R. A. de Groot, and G. A. de Wijs, *Phys. Rev. B* **79**, 125117 (2009).